Polymer 49 (2008) 5683–5691

Contents lists available at ScienceDirect

Polymer

journal homepage: www.elsevier.com/locate/polymer

Dispersing hairy nanoparticles in polymer melts

Xiaorong Wang*, Victor J. Foltz, Mindaugas Rackaitis, Georg G.A. Böhm

Bridgestone Americas, Center for Research and Technology, 1200 Firestone Parkway, Akron, OH 44317, United States

ARTICLE INFO

Article history:
Received 19 August 2008
Received in revised form 9 October 2008
Accepted 13 October 2008
Available online 1 November 2008

Keywords:
Hairy nanoparticles
Polymer melts
Phase behavior

ABSTRACT

The dispersion of hairy nanoparticles in polymer melts of chemically identical chains was investigated as a function of both molecular weight and volume fraction. Here we provide conclusive evidence that the shape of the phase diagram is determined primarily by the ratio of the chain length of the polymer melt to the chain length of the polymeric shell structure (or hair) of the core/shell nanoparticles, and that the phase behavior of different hairy particles in various polymer melts can be superimposed into one universal graph. Other factors, including the hair density and the particle diameter, are not nearly as significant as the above-noted ratio in this phase separation. In addition, we show that there is a strong connection between the rheological dynamics of the particle-filled system and the thermodynamics of the phase separation behavior. The shear-induced nonlinearity in the particle-filled system appears to display features of a singularity near the phase transition point.

1. Introduction

Polymers reinforced with nano-sized particles represent one of the oldest of composites and have important applications [1]. Their physical properties depend strongly on the microscopic interactions between the dispersed particles (or fillers) and the phase stability of particles in the polymer matrix [2–4]. One example is in tire tread compounds, decreasing the interactions between filler particles can frequently reduce the rolling resistance and improve the vehicle gas mileage; while, increasing the filler–filler interactions in a tread rubber can sometime improve tear strength and traction performance. Therefore, achieving a good understanding of the interactions between the filler particles and the phase behavior of the particles in a host matrix is crucial [3] before a commercial introduction of the material as a final product.

Recently core/shell polymeric nanoparticles have attracted enormous attention in rubber applications [5–25]. This interest is largely based on the fact that nanoparticles having hairy shell and solid core structures might offer superior physical properties in rubber applications [10]. The underlying picture is that the hair molecules may act like flexible bridges that link the hard reinforcing core at one end and entangle the soft host polymer matrix at another end. After vulcanization, all of the shell molecules may be covalently bonded to the rubber network, and thus provide significantly improved reinforcement. In addition, the hairy nanoparticles can be easily modified and tailored through appropriated design of the particle structures for particular applications [9–13], including the core hardness, the shell thickness, the core/shell interface, the hair molecule density, surface functional groups, etc.

Beside the importance for applications, the study of the microscopic behavior of the hairy nanoparticles in a polymer melt is of fundamental interest. Theoretically it has been recognized for some time that the interactions between polymer flat brushes in the presence of free polymers of the same microstructures is primarily determined by entropy-driven forces [26–35], and the interaction strength can be adjusted by varying the size and the concentration of the free polymers or the grafted brush molecules [30–35]. While those studies appear to suggest that the interactions between brushes could be unified within few molecular parameters, it is not clear if this inclusion would allow for a proper description of the phase behavior of hairy nanoparticles in polymer melts using a similar unified picture. There were several experimental studies which discussed the phase behavior of micro- and submicro-sized colloidal particles carrying attached polymer chains in dilute or semi-dilute solutions [36–39]. However, for polymer melts, except for very few reports [40–42] that discussed the stability of this system, there is no experimental data available for a critical examination of the fundamentals as described. Also, theoretical studies discussed the interactions between particles mostly based on systems of flat brushes [41–49]. The equilibrium statistics of polymers grafted on convex surfaces has only been considered in recent years [50–52], where a proper treatment of the exclusion zone in spherical brushes is still lacking [52]. As a result, the effects of interactions between the convex curved brushes are less understood than those between flat brushes. In this contribution we report on an investigation of the phase behavior of polymeric

* Corresponding author. Tel./fax: +1 330 379 7330.
E-mail address: wangxiaorong@bfusa.com (X. Wang).

0032-3861/$ – see front matter © 2008 Elsevier Ltd. All rights reserved.
doi:10.1016/j.polymer.2008.10.019

hairy nanoparticles in polymer melts of chemically identical chains as a function of both molecular weight and volume fraction. The nanoparticles investigated are slightly larger than the dimension of the grafted chains.

2. Materials and experiments

Butadiene in hexane (about 22 wt% butadiene), styrene in hexane (about 33 wt% styrene), pure hexane, and *n*-butyllithium in hexane (1.6 M in hexane) were used as-supplied under nitrogen from the Firestone Polymer Company. Technical grade divinyl benzene (Aldrich) containing mixture of isomers (80%) as well as isomers of ethylvinylbenzene was passed through a column comprising a proprietary activated alumina based inhibitor remover (Aldrich) and calcium hydride under nitrogen before use. Other solvents such as isopropanol and acetone, and the antioxidant butylated hydroxytoluene (BHT) were used as-received. A 7.6-l high-pressure reactor (Chemineer Inc.) equipped with a pitch blade impeller was used for the synthesis work.

Polymeric nanoparticles comprising polybutadiene (PBD) hairy shell and crosslinked polystyrene (PS) core were synthesized using anionic polymerization. In the synthesis, the reactor was first charged with hexane and butadiene monomer. The batch was then heated to 57 °C. After the temperature was stabilized, the polymerization was initiated by adding a desired amount of *n*-butyllithium in the absence of any modifier. After the polymerization of butadiene was accomplished, a small amount of the solution was drained from the reactor and then deactivated using isopropanol for analysis. The reactor was then charged with a desired amount of a blend of styrene and divinyl benzene (or DVB) at a ratio of about 70/30. Because the two vinyl groups in DVB have different reactivities, the initially formed polymer was a PBD-*b*-(PS-*co*-DVB) diblock-like copolymer. In a hexane solution of about 12% solid, this living diblock aggregated through self-assembly forming spherical micelles, with the styrene block directed toward the center of the micelle and the butadiene block as tail extending therefrom. This occurred because the polystyrene blocks of the copolymer were largely insoluble in hexane whereas the polybutadiene blocks were very soluble in this solvent. Further reaction of the second vinyl group in the divinyl benzene unit crosslinked the PS core, as illustrated in Fig. 1. The detail synthesis procedure has been described elsewhere [10]. After the reaction is completed, the batch was discharged into a 40/59/1 blend of isopropanol, acetone and BHT. The product was precipitated from the solution, filtered, and was finally dried in vacuum at 50 °C.

Table 1 shows the characteristics of two polymeric nanoparticles (MNP-1 and MNP-2) that were prepared for the present study. The molecular weights and sizes of the nanoparticles in solution were determined using an 18-angle light scattering detector (Dawn Heleos) from Wyatt Technology. The detector was connected online to a gel permeation chromatography that was from Waters HSGPC

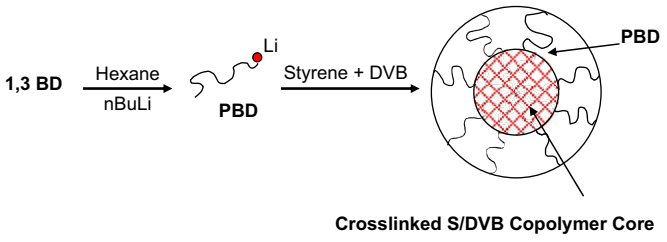

Fig. 1. A schematic drawing for the synthesis of polymeric nanoparticles comprising polybutadiene (PBD) hairy shell and polystyrene (PS) crosslinked core in hexane using an anionic polymerization process.

Equipment. Tetrahydrofuran (THF) was used as the solvent. The nanoparticles were also examined in the dry state using electron microscopy. There was a considerable difference between the particle size measured in dry state and that measured in THF solution. This discrepancy was due to the fact that the shell polymer chains were able to swell in THF. The number of PBD chains per particle in the shell was calculated using the molecular weight of particles, the core-shell composition, and the shell PBD molecular weight. The shell PBD molecular weight was measured from the intermediate product that was taken from the reactor after the first synthesis step, as described previously. MNP-1 and MNP-2 are similar in core size, but differ significantly in their shell molecules.

Table 2 lists 21 linear polybutadienes (PBD-1 to 21) that were prepared for the present investigation. These mono-dispersed PBDs were synthesized by anionic polymerization using the same reactor, solvent, and temperature profiles that were used to prepare the shell portion of the nanoparticles. Under such conditions, the synthesized PBD polymers were chemically identical to the shell molecules of the nanoparticles. The molecular weights of these PBDs were analyzed by gel permeation chromatography using Waters HSGPC equipment. The GPC column was calibrated using polystyrene standards. Tetrahydrofuran was used as the solvent. The microstructure such as vinyl content, etc. was determined by H ^{1}NMR measurements. A Varian Gemini 300 NMR spectrometer was used for the analysis. The *cis*- and *trans*-BR contents (not listed) were typically 50 to 50 for a PBDs made from the anionic polymerization. The glass transition temperatures for these low-vinyl PBD polymers (not listed) were about −90 °C.

Blends of the PBD-shelled nanoparticles and the linear PBDs of various ratios were prepared by dissolving the particles and the PBDs in hexane at 23 °C in sealed flasks. The particles and the PBDs were at first weighed into flasks on a balance with 10^{-4} g accuracy. Then, 0.1% BHT (antioxidant) was added to the flask for stabilization. After that hexane solvent was charged to the flask. The amount of hexane added to the flask was about 9 times the amount of the solids. Complete dissolution took place within 12 h under moderate stirring. Once the solutions were clear, they were poured into flat pans and dried in air at 23 °C. After the hexane was evaporated, the blends were degassed under vacuum at 50 °C for 12 h. The degassed blends were then transferred into optical glass vials and were equilibrated at 23 °C for at least two weeks before making measurements.

Turbidity measurements of the nanoparticle/PBD blends were carried out with a turbidimeter (DRT-15CE) from USEPA & HF Scientific. The turbidity was recorded in Nephelometric Turbidity Units (NTU). Standard formazin solutions certified by HF Scientific were used for the calibration. Optical glass vials (Liquid Scintillation) with 28 mm outside diameter and 55 mm height from Wheaton Scientific were used for holding the samples. Before the vial was placed into the equipment, the outside surface of the vial was carefully cleaned with a lint free wiper moistened with THF and hexane. A measurement was taken from an average of 3–5 readings. Reported data is within a 5% error bar.

Electron microscopic (EM) observations were carried out with a Hitachi S-4800 electron microscope in STEM mode. Thin films were sliced from a sample using a Leica Emfcs Ultracut UCT Ultramicrotome at about 2.5 mm/s. The slicing was done at about −120 °C. The sliced films were then collected on an amorphous carbon-coated copper micro-grid and stained with OsO_4 prior to the electron microscopy observation. Atomic force microscopy (AFM) observation was carried out with a Dimension 3000 microscope made by Veeco Instruments. The AFM was used in tapping mode with an etched silicon tip on a fresh sample surface. The measurement was carried out at 23 °C in air having 60% humidity.

Measurement of dynamic moduli (G' and G'') of the blends was carried out at various strain amplitudes using a Rheometrics

Table 1a
Characterization of poly(styrene/butadiene) nanoparticles studied.

Sample ID	Particle radius in dry state[a] R_n (nm)	Particle radius in THF[b] R_n (nm)	Polydispersity of particle[b] R_w/R_n	Particle molecular weight, M_n[b] (g/mol)	Polydispersity of particle MW[b] (M_w/M_n)	Particle purity[c] (%)	PBD shell/x-PS core (ratio)
MNP-1	8.5	12.0	1.12	8.841×10^5	1.14	98.7	67/33
MNP-2	9.8	14.6	1.04	9.538×10^5	1.09	99.1	80/20

ARES strain-controlled rheometer equipped with dual 200 and 2000 g cm force rebalance transducers. Strain sweeps were made at 1 Hz and 30 °C. A cone and plate geometry was used to ensure a homogeneous strain field. The plate diameter/cone angle combination used was 25 mm/0.02 rad. After a polymer blend was loaded between the core and plate, the material was allowed to equilibrate at 30 °C, 1 Hz and 0.01% strain. After the normal force relaxed to zero, a strain sweep from 0.01% to 30% was performed in logarithmic increments. The strain during oscillatory shear was varied as $\gamma \sin \omega t$, where γ is the strain amplitude and ω is the angular frequency.

3. Results

Fig. 2 is a photograph showing the typical phase evolution of the hairy nanoparticle/PBD blend at 23 °C as a function of PBD molecular weight, M_f, where the subscript "f" stands for the free PBD. In the photograph, the nanoparticle studied is MNP-1 and the concentration is 10% by volume. The characteristic data of MNP-1 is listed in Table 1. It has a core/shell structure. The core is made of highly crosslinked PS that contains 33% of DVB. The shell is composed of 66 chains of mono-dispersed PBD of molecular weight $M_g = 8780$ g/mol that are end grafted to the solid core surface. The subscript "g" stands for the grafted PBD chains. As one can see in Fig. 2, when the free PBD is made of short polymer chains (e.g., when $M_f < 15{,}000$ g/mol), we have blends that are all transparent, which suggests that the interactions between particles are repulsive. When the free PBD is made of long polymer chains (e.g., when $M_f > 25{,}000$ g/mol), we have blends that are all opaque, which indicates that the interactions between the particles are attractive. Between the two extremes there is a clear transition and the phase separation can be easily observed with a naked eye.

Fig. 3 presents the quantitative turbidity measurements for the series shown in Fig. 2. The turbidity always increases with increasing free PBD M_f. However, over a range of $0 < M_f < 2M_g$ the increment rate is noticeable slow. Then, the turbidity suddenly rises rapidly with increasing M_f when $M_f > 2M_g$. The transition can be easily located by a clear break in the curve at $M_f^c = 21{,}500$ g/mol. This result suggests that the chain length of the free PBD melts is one of the control parameters that govern the aggregations of the hairy particles in these blends. Increasing M_f in fact drives a phase separation.

Table 1b
Characterization of PBD shell microstructure.

Sample ID	Molecular weight of PBD in shell[c] Mn (g/mol)	Polydispersity of PBD in shell[c] (M_w/M_n)	1,2-Addition[d] (%)	1,4-Addition[d] (%)	Number of PBD chains per particle[e]
MNP-1	8780	1.09	8.4	91.6	66
MNP-2	18,060	1.05	8.7	91.3	42

[a] Measured by transmission microscopy in dry state.
[b] Measured by GPC-light scattering equipment in THF solution.
[c] Measured by GPC.
[d] Measured by NMR.
[e] Calculated using molecular weights and core/shell compositions.

Fig. 4 shows the microscopic evidence for the phase separation observed by transmission electron microscopy (TEM). The nanoparticle studied is MNP-1 and the concentration of nanoparticles is 10% by volume. Image 4a shows a blend in which the free PBD has a molecular weight $M_f = 14{,}020$ g/mol. The system is still in the one-phase regime and the particles are well separated in the blend. Image 4b shows a blend in which the free PBD has a molecular weight $M_f = 22{,}570$ g/mol. The system is now near the phase-transition critical point. Large fluctuations in particle density can be seen from point to point in the system. The fluctuations result in the formation of networks of a correlation length of hundreds of particles. Image 4c shows a blend in which the free PBD has a molecular weight $M_f = 57{,}030$ g/mol. The system has fully entered the two-phase regime. The nanoparticles aggregate together as big micro-sized droplets and thus light scattering significantly increases. The transition between those two regimes is well marked. This shows that the nanoparticles can either form individual separate particles in the blends or associate as macroscopic droplets of high nanoparticle concentrations, depending on M_f. Thus, M_f in this system acts like an "effective temperature", as temperature does in the phase separation of a typical binary system of small molecules. Our AFM results on these samples (not shown) are consistent with the TEM analysis shown in Fig. 4.

Fig. 5 displays the effect of the shell molecular weight M_g of the nanoparticles on the phase transition. In this plot, the phase behavior of the particle MNP-2 is compared to that of MNP-1, and the particle concentration is 10% by volume. As described earlier, MNP-1 and MNP-2 have closely equal core size, but differ in M_g. For MNP-1 with $M_g = 8780$ g/mol the phase transition occurs at $M_f^c = 21{,}500$ g/mol. However, for MNP-2 with $M_g = 18{,}060$ g/mol the phase separation is considerably delayed until the free PBD molecular weight M_f reaches above 57,000 g/mol. Accordingly, an increase of the shell molecular weight M_g of the nanoparticles

Table 2
Characterization of linear polybutadiene used.

PBD#	GPC M_n (g/mol)	M_w/M_n	NMR vinyl (%)	1,4-Addition (%)
PBD-1	3460	1.22	9.2	90.8
PBD-2	3500	1.23	9.3	90.7
PBD-3	7010	1.14		
PBD-4	8680	1.10	8.8	91.2
PBD-5	9780	1.09	8.8	91.2
PBD-6	10,950	1.08	8.6	91.4
PBD-7	14,020	1.07	8.7	91.3
PBD-8	17,080	1.06		
PBD-9	18,900	1.05	8.7	91.3
PBD-10	22,570	1.05	8.6	91.4
PBD-11	28,540	1.04		
PBD-12	31,630	1.04		
PBD-13	37,390	1.03		
PBD-14	44,370	1.03		
PBD-15	50,090	1.03	8.6	91.4
PBD-16	59,840	1.03		
PBD-17	57,030	1.03	8.6	91.4
PBD-18	58,900	1.03		
PBD-19	110,350	1.06	8.7	91.3
PBD-20	135,890	1.10		
PBD-21	145,320	1.11		

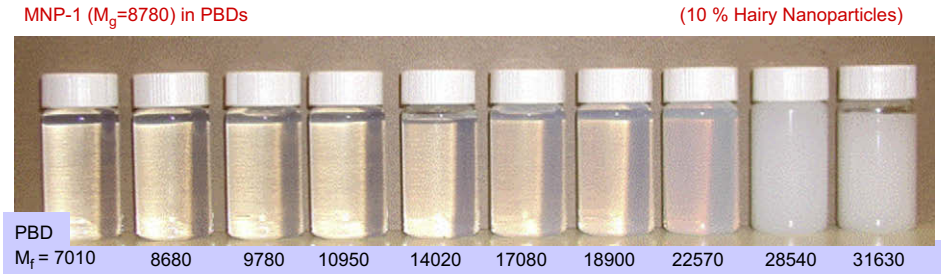

Fig. 2. A photograph of the phase evolution of hairy nanoparticle/PBD blends at 23 °C as a function of the free PBD molecular weight M_f. The nanoparticle studied is MNP-1 and the concentration is 10% by volume.

increases the critical molecular weight M_f^c at the phase transition. The increments are proportional to each other.

Fig. 6 displays the concentration dependence of the phase transition of the nanoparticle MNP-1 in various polybutadienes (PBDs). The boundary between the one-phase regime and the two-phase regime is marked by the critical molecular weight M_f^c at the phase transition as a function of the particle concentration. The value of M_f^c is determined by the curve breaking in the turbidity measurements (as that shown in Figs. 3 and 5). The minimum in the phase transition boundary occurs at a decidedly low particle concentration. The great difference in the size of the particle and that of the free PBD molecule may be responsible for the highly asymmetric phase diagram. One interesting observation is that when the concentration is below 60%, the phase boundary is relatively insensitive to a change of concentration, whereas above 60% the phase boundary curves up and increases rapidly with increasing concentration.

Fig. 7 presents a comparison between the phase diagram of MNP-1 and that of MNP-2. Despite that the two particles differ significantly in shell molecular weight and the grafting density, it is remarkable to note that the phase diagrams for MNP-1 and MNP-2 have pronounced similarity in shape. In fact the two boundary lines from different hairy nanoparticles and polymer melts can be superimposed into a universal curve if the ratio M_f^c/M_g is used as the dependent variable for plotting, as shown in Fig. 8. The onset of the phase separation is located when the chain length of the polymer melt is about twice as large as the chain length of the polymer hair on the nanoparticles. The topology of the phase diagram is determined primarily by the ratio of the two chain lengths.

Although using M_f^c/M_g as the dependent variable has resulted in the phase boundary lines from different hairy nanoparticles to be closely superimposed into one universal curve, there still is some disparity between the curve for MNP-1 and the curve for MNP-2.

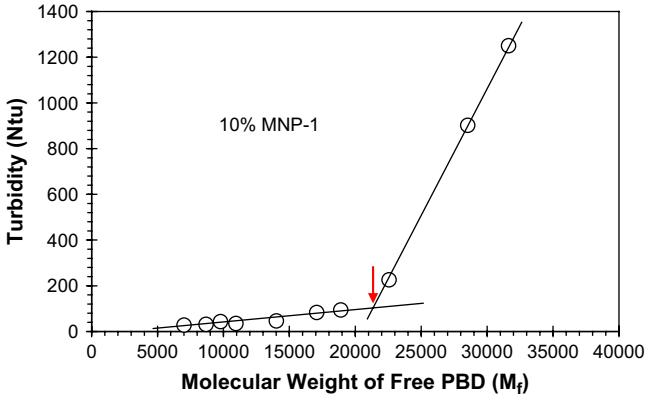

Fig. 3. Turbidity measurement of hairy nanoparticle/PBD blends at 23 °C as a function of the free PBD molecular weight M_f. The nanoparticle studied is MNP-1 and the concentration is 10% by volume.

A perfect matching of the two curves is possible only if a shift parameter κ is introduced. Fig. 9 shows a plot where $\kappa(M_f^c/M_g)$ is used as the dependent variable for plotting with $\kappa = 1.2$ for MNP-2 and MNP-1 as the reference. Fundamentally, there may be some physical significance of the parameter κ, which could be related to the surface curvature and the hair density of the nanoparticles.

Fig. 10 shows the impact of phase separation on the rheology of the system. Here we see that the mechanical response of the system to shear is essentially linear when the molecular weight of the free PBD (M_f) in the blend is low, and the storage modulus G' is constant over the strain range from 0 of to 20%, As M_f increases, the mechanical response of the blend becomes nonlinear. The nonlinearity intensifies when the system approaches the phase separation point, reaching a maximum at the locus of the phase separation. It is noteworthy that a further increase in M_f causes the mechanical response of the system to become more linear again. As the system enters deeply into the two-phase regime, the material resumes the linear behavior as it does in the one-phase regime. Surprisingly, the rheological dynamics of particle-filled systems has a direct connection to the thermodynamics of the system.

The sensitivity of the phase behavior to temperature changes was also investigated for these blends of hairy nanoparticles and PBD melts (over 200 samples). In one experiment these samples were kept in hot water at 80 °C for one week. In another experiment these samples were placed in a freezer at −20 °C for one year. Since the glass transition temperatures of the PBD polymers were about −90 °C, the samples should be in a liquid state at −20 °C and thus would be fairly equilibrated after a one-year interval. Only visual observations (with the naked eye) were made because the turbidimeter was not suitable for measurements at temperatures other than ambient temperature due to calibration difficulties. Nevertheless, our observation shows that the transition points in those blends and the phase diagrams for the MNP-1 and MNP-2 systems were not at all sensitive to the temperature change. No experiments were performed above 80 °C because long-term storage may result in crosslinking of the PBD polymers.

4. Discussion

4.1. Phase behavior and interaction potential

To interpret the experimental results, we need to know more about the nature of the interaction between the nanoparticles and the free polymers. It would be nice if statistical thermodynamics could be derived entirely from the molecular parameters that we already know, such as the polymer chain length and the hair density. Unfortunately, the problem raised by these interactions is rather complex when two hairy nanoparticles approach each other in the presence of free polymer. At present no exact analytical solution for this problem is available. Computer simulations may provide numerical solutions, however, it is difficult to extract the

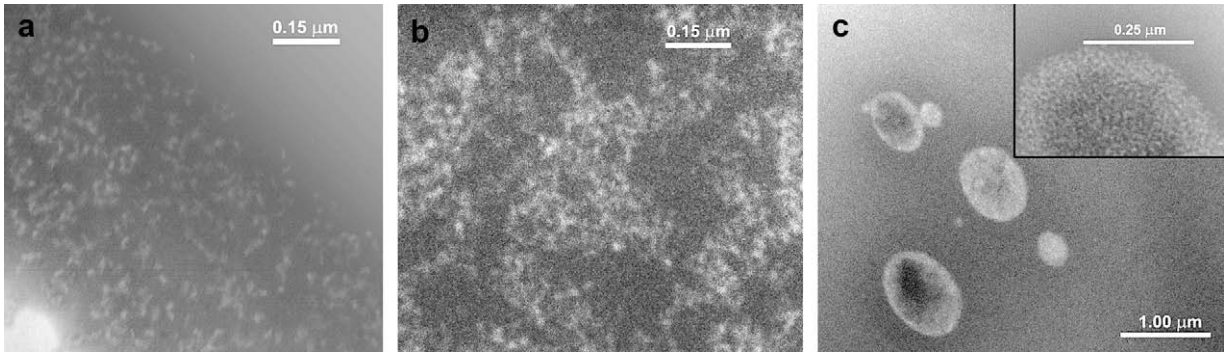

Fig. 4. TEM images of the phase separation of the hairy nanoparticle/PBD blends. The nanoparticle studied is MNP-1 and the concentration is 10% by volume. Image (a) shows a blend in which $M_f = 14{,}020$ g/mol. The system is still in the one-phase regime. Image (b) shows a blend in which $M_f = 22{,}570$ g/mol. The system is close to the phase-transition critical point. Image (c) shows a blend in which $M_f = 57{,}030$ g/mol. The system is in the two-phase regime.

key features that govern the physics. Since our main concerns are the properties and the criteria for the occurrence of phase separation, we use an approach similar to the one used by others in dealing with polymer brushes [30–35] and polymer micelles [40–49]. As shown in the following discussion, it is possible to explain the observed equilibrium behavior of hairy nanoparticles in polymer melts using a simple physical model without involving complicated mathematics.

Supposing two spherical particles of core radius, R_0, and grafted layers with equilibrium thickness, L, separated by a distance of z, one can distinguish three domains that are specified by the relative magnitudes of the parameters z, R_0 and L. (1) When $z > 2(R_0 + L)$, the separation between the two particles exceeds twice the grafted layer thickness and core radius, the particles are unable to interact. Close approach of the particles in this domain involves no free energy change. (2) When $z \approx 2(L + R_0)$, the distance between the particles is about twice the surface layer thickness and core radius, the free polymer concentration ϕ_f in the interface undergoes changes. Thus when the two particles closely approach each other, the interface between the grafted layer and the free polymer matrix (or the melt) gradually vanishes. Consequently, the free energy of the interaction in this domain derives from the loss of the interface energy, which yields an attractive potential well. This is the attractive domain. (3) When $z < 2(L + R_0)$, the separation distance is less than twice of the grafted layer thickness and core radius, the grafted polymer layers undergo a compression. This is the repulsive domain.

Now let us consider the case that only one hairy particle is placed in a polymer melt of chemically identical chains with a degree of polymerization N_f. The free polymer in the melt may penetrate the grafted layer. The interpenetration profile can be schematically depicted in Fig. 11. The concentration of the grafted polymer ϕ_g is expected to be near 1 inside and falls to zero in a relatively thin interpenetrated layer, ξ, between the grafted layer and the surrounding free polymer. Using three linear lines we simplify the concentration profile to be three linear regions, i.e., the dry brush region, the interpenetrated region, and the free polymer region.

Then we use the ground-state dominance method of Edwards [53] to calculate the local penetrating thickness of the free polymer chains into the grafted layer. The ground-state dominance theory describes the configurational probability of the free polymer chains by a diffusion equation:

$$\frac{a^2}{6}\nabla^2\Psi - U\Psi = 0 \tag{1}$$

where the free polymer concentration $\phi_f = \Psi^2$ and U is the mean field potential. Equation (1) may also be written in a different form using ϕ_f as dependent variable and z as independent variable.

$$\frac{a^2}{12}\nabla^2\phi_f - \frac{a^2}{24}\frac{1}{\phi_f}\left(\frac{d\phi_f}{dz}\right)^2 - U\phi_f = 0 \tag{2}$$

where a is the monomer size in the polymer.

The potential U is composed of two components u_1 and u_2, where u_1 is the chemical potential that can be derived from the Flory–Huggins theory [54]. The leading term in the chemical potential u_1 is

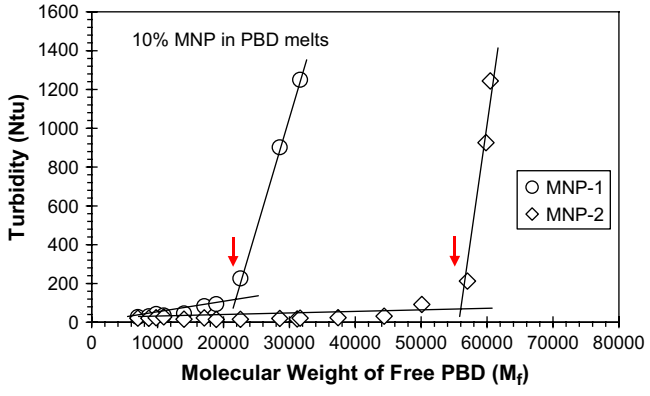

Fig. 5. Effects of shell molecular weight M_g of the nanoparticles on the phase transition. For MNP-1 with $M_g = 8780$ g/mol the phase transition occurs at $M_f^c = 21{,}500$ g/mol. For MNP-2 with $M_g = 18{,}060$ g/mol the phase separation occurs at $M_f^c = 57{,}000$ g/mol. The particle concentration is 10% by volume.

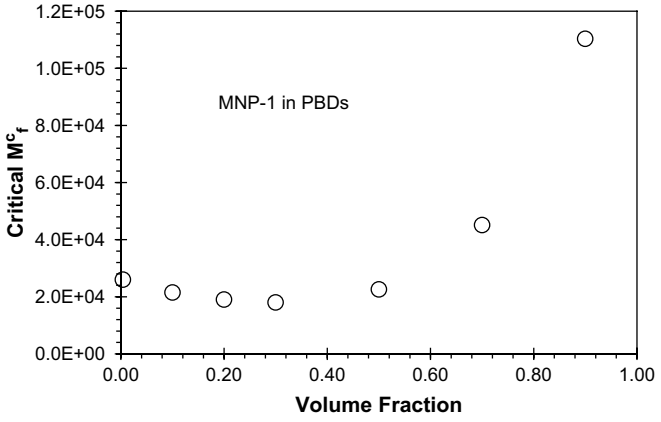

Fig. 6. Critical molecular weight M_f^c of free PBD at the phase transition as a function of the particle concentration: the phase diagrams of MNP-1 in PBD melts. The first data point on the left side of the chart was measured at particle concentration of 0.2%.

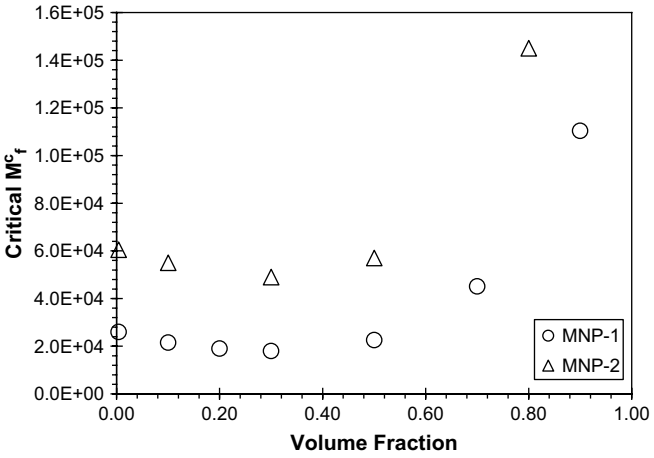

Fig. 7. Critical molecular weight M_f^c of free PBD at the phase transition as a function of the particle concentration: a comparison between the phase diagrams of MNP-1 and MNP-2. The phase diagrams for MNP-1 and MNP-2 have pronounced similarity in shape, despite that they differ significantly in shell molecular weight and graft density.

$$u_1 = -\frac{1}{N_f}\ln\phi_f \tag{3}$$

The potential energy u_2 arises from the repulsive interaction of a given chain with others in the grafted layer. For a flat surface, we may use the asymptotic parabolic form of u_P, as proposed by Witten et al. [30–32] based on the harmonic spring argument, $u_P = \pi^2 a^{-2}/8N_g^2(L^2 - z^2)$, where N_g is the degree of polymerization of polymer chains that are terminally grafted to the particles. However, for a spherical (or convex) surface, the outer profile becomes much more complicated. As shown by Ball et al. [50], there are two distinct regions inside the grafted layer: an exclusion zone ($z < z_Q$) with no free chain ends and a relaxed region ($z_Q < z \le L$) with chain end distributed. A proper treatment of the exclusion zone in spherical brushes is still lacking. So far there is no complete solution for polymer grafted on a spherical surface.

Although the situation deep inside the brushes is complicated for convex surfaces, the situation near the open surface is relatively simple. Both the variational analysis by Li and Witten [51] and the numerical calculations by Belyi [52] show that near the open surface the density profile still maintains the same parabolic structure as that found in flat and concave brushes. At present, our best understanding of this convex problem is that for most cases

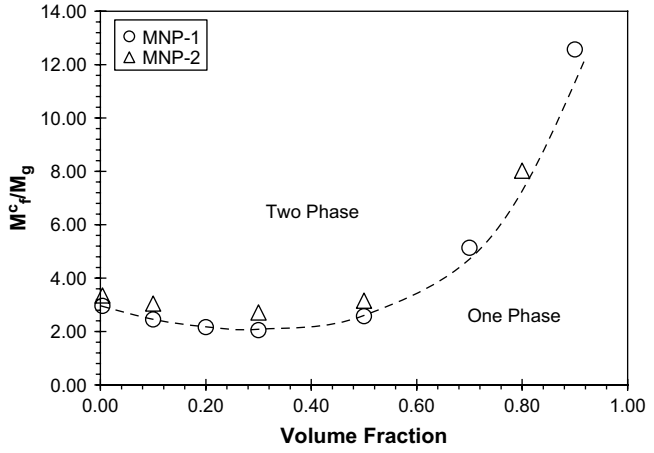

Fig. 8. Normalized phase diagram of hairy nanoparticle/PBD blends when the ratio M_f^c/M_g is used as the dependent plotting variable. Phase boundary lines from different hairy nanoparticles are closely superimposed into one universal curve.

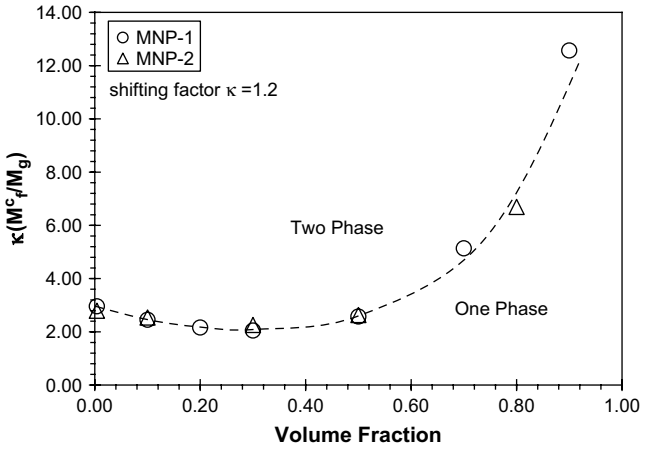

Fig. 9. Normalized phase diagram of hairy nanoparticle/PBD blends when $\kappa(M_f^c/M_g)$ is used as the dependent plotting variable, where $\kappa = 1.2$ a shift parameter.

when the exclusion zone is a small fraction of the grafted layer thickness, the width of the exclusion zone and the effects that arise from it vary as the exponential of minus the radius of curvature over brush thickness. For instance, the potential at the boundary of the exclusion zone, u_Q, can be related to the potential at a flat interface [50], u_P, via

$$\frac{\beta R_0}{L} = \alpha^{-1}\ln\left(\frac{u_P}{u_P - u_Q}\right) \tag{4}$$

If extending this expression for u_Q beyond exclusion zone (i.e., $z > z_Q$) to the open surface, one would obtain

$$u_2 = [1 - \alpha\exp(-\beta R_0/L)]u_p = [1 - \alpha\exp(-\beta R_0/L)]\frac{\pi^2}{8a^2N_g^2}\left(L^2 - z^2\right) \tag{5}$$

where $\alpha = 0.71$ and $\beta = 0.5$ are constants [52]. Although this exponential correction is only formally derived based on an argument of weak curvature limit, numerical calculations [50,52] show that this correction is applicable over a wide range from the weak curvature when $R_0 \gg L$ up to the intermediate curvature for $R_0 \approx L/3$. Thus, near the extremity of the interpenetrated layer as it is shown in Fig. 11, we may approximate u_2 as

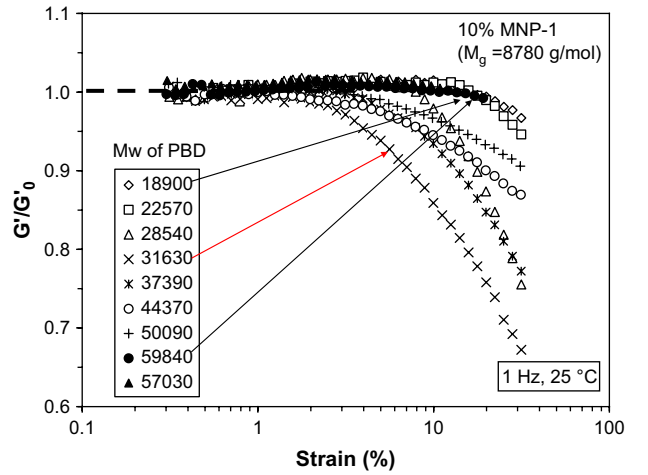

Fig. 10. Dynamical modulus (G') of the system as a function of the free PBD molecular weight M_f in the blends. The nanoparticle studied is MNP-1 and the concentration is 10% by volume. The strain-induced nonlinearity in the particle-filled system appears to display features of a singularity near the phase transition point.

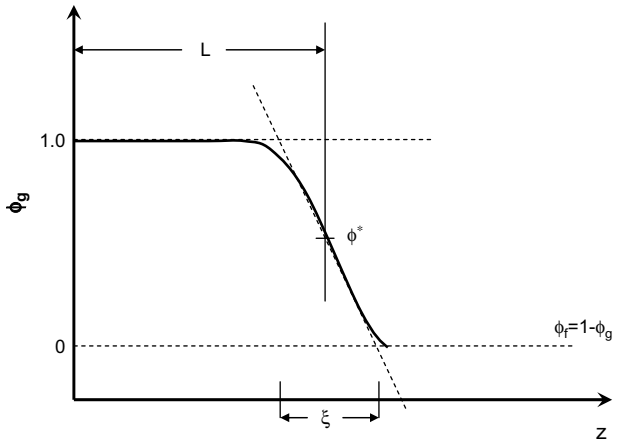

Fig. 11. A schematic drawing of the concentration profile of the grafted polymer ϕ_g as a function of distance z that extends from the core surface. The profile can be simplified using three linear lines.

$$u_2 = u(L) + \left.\frac{\partial u_2}{\partial z}\right|_L \xi = \upsilon \frac{\pi^2 L}{4a^2 N_g^2}\xi \tag{6}$$

where $\upsilon = 1 - \alpha\exp(-\beta R_0/L)$ and takes care of the curvature of the hairy particles. The effect that arises from the curvature is noticeable but small. The value of υ varies from 1 for a flat surface (as $R \gg L$) to about 0.6 for convex surfaces of intermediate curvature as ($R \approx L$). The limit of $R \ll L$ for stars is not the interest of this study and will not be discussed here. Our main concerns are nanoparticles of finite and reinforcement cores that are slightly larger than the dimension of grafted chains.

Inserting Equations (3) and (6) into Equation (1) and taking account the three-lined linear profile as shown in Fig. 11, we may write the diffusion Equation (2) in the interpenetrated layer in the following form:

$$\frac{a^2}{12}\left(\frac{1}{\xi}\right)^2 - \frac{\pi^2 \upsilon L}{8a^2 N_g^2}\xi + \frac{\phi^* \ln\phi^*}{N_f} = 0 \tag{7}$$

where we take $\phi^* = 0.5$, the middle point in the linear profile. When N_f is large, the last term on the left side of Equation (7) vanishes, and we thus get

$$\xi = \left(\frac{2a^4}{3\pi^2\upsilon}\frac{N_g^2}{L}\right)^{1/3} \tag{8}$$

For flat brushes as $\upsilon = 1$, this result agrees well with that obtained by Leibler and Ajdari [55]. For convex surfaces because $\upsilon < 1$, the results of Equation (8) suggest that a curved brush layer is more penetrable than a flat layer as may be expected from the potential profile of such layers.

Now let us examine the interaction energy for the case when two grafted plates closely approach each other: $F(z) = F_g(z) - F_g(\infty) + F_f(z) - F_f(\infty)$, where "$\infty$" represents the excess free energy at infinite separation. The subscript "g" represents the grafted polymer contribution and the subscript "f" represents free chain contribution. We note that as the two polymer-grafted surfaces approach each other the free polymer concentration ϕ_f in the interface undergoes changes. This change in the interface concentration ϕ_f reduces the free energy that favors mixing. Therefore, the attractive potential arises mainly from the free chain contribution F_f. The brush contribution typically produces repulsive force. Accordingly, the attractive potential, which is the most interesting, is determined by

$$F_{attr} \cong F_f(2L) - F_f(\infty) \tag{9}$$

Following the asymptotic approximation proposed by Broseta et al. [56] and also used by Semenov [41], the value of F_{attr} is given by

$$F_{attr} = -\int_{\infty}^{2(L+R)} \left\{\frac{a^2}{12}\nabla^2\phi_f - \frac{a^2}{24}\frac{1}{\phi_f}\left(\frac{d\phi_f}{dz}\right)^2 + \frac{\phi_f \ln\phi_f}{N_f}\right\} dz \tag{10}$$

We may simplify the integration using the three-lined linear profile as shown in Fig. 11. The result is

$$F_{attr} = -\frac{a^2}{24}\frac{1}{\xi} - \frac{\phi^*\ln\phi^*}{N_f}\xi \tag{11}$$

Equation (11) predicts that the attractive force depends on the size of polymer chains. For long polymer melts ($N_f \gg 1$) the interaction is always attractive. However, as N_f decreases and the interpenetrated layer ξ increases, the interaction may become repulsive. The critical value of N_f is,

$$N_f^c = -24\phi^*\ln\phi^*\left(\frac{\xi}{a}\right)^2 \cong 8\left(\frac{2a}{3\pi^2\upsilon}\frac{N_g^2}{L}\right)^{2/3} \cong 1.4\left(\frac{aN_g^2}{\upsilon L}\right)^{2/3} \tag{12}$$

The shell thickness L can be estimated by using a simple geometrical argument. Let us assume that the grafting density is σ and the average distance between two grafted sites is given by $D = a\sigma^{-1/2}$, where a is the monomer size. Thus, the number of terminally grafted chains per unit area is σa^{-2}. At sufficiently low σ, the grafted chains do not overlap, the thickness of the grafting layer is given by an ideal coil size $aN_g^{1/2}$ as long as $N_f > N_g^{1/2}$. This regime is limited by the condition of $(aN_g^{1/2})^2\sigma a^{-2} < 1$ or $\sigma < N_g^{-1}$. If the density σ of the grafted polymer is beyond the limit, the grafted chain begins to overlap, and this may lead to stretching [57]. Thus, the phenomenon of the grafted polymer chains stretching themselves may occur at a very low grafting density, i.e., at $\sigma > N_g^{-1}$ when N_g is large.

Let us consider an isolated nanoparticle with a core of radius R_0 and a shell of thickness L. Assuming that the shell contents n terminally grafted polymer chains and that the interpenetration of the free polymer is small, we may write

$$\frac{4}{3}\pi R^3 - \frac{4}{3}\pi R_0^3 = a^3 n N_g \tag{13}$$

where R is the overall radius of the particle and thus $L = R - R_0$. Equation (13) can be re-written into the following form

$$\left(\frac{L}{R_0}\right)^3 + 3\left(\frac{L}{R_0}\right)^2 + 3\left(\frac{L}{R_0}\right) - 3C = 0 \tag{14}$$

where $C = a\sigma N_g/R_0$. For the cubic equation, the procedure to obtain its roots is standard, and the result is

$$\frac{L}{R_0} = \left(\frac{3a\sigma N_g}{R_0} + 1\right)^{1/3} - 1 \tag{15}$$

Equation (15) predicts three interesting situations for the hairy shells of the nanoparticles. First, when $L \ll R_0$, this equation predicts a simple scaling relation $L/R_0 \approx (3a\sigma N_g/R_0)^1$. The grafted polymers in this case will behave as if they are attached to a planar surface and completely stretched. The grafted layer has a thickness of $L = a\sigma N_g$. Second, when $L \gg R_0$, the grafted polymer in this case will act as if they are attached to a point. The scaling relation changes to $L/R_0 \approx (3a\sigma N_g/R_0)^{1/3}$, where L scales as 1/3 power over N_g. Third, for the case when L is of a similar order of magnitude as R_0 (or $L \approx R_0$), equation is reduced as

$$\frac{L}{R_0} \cong \left(\frac{a\sigma N_g}{R_0}\right)^{1/2} \tag{16}$$

Equation (16) is asymptotically correct as long as $L \approx O(R_0)$ and closely represents the real situation at hand. Since the size of a polymer chain (for $N \sim 100$ and $a \sim 5A$) is about 5 nm, Equation (16) should be applicable for a nanoparticle of core size R_0 from 2 nm to 20 nm. Substituting Equation (16) into Equation (12), we obtain

$$N_f^c \cong 1.4\left(\frac{a}{R_0\sigma\upsilon^2}\right)^{1/3} N_g \quad \text{or} \quad \frac{N_f^c}{N_g} \cong 1.4\left(\frac{a}{R_0\sigma\upsilon^2}\right)^{1/3} \tag{17}$$

We now see that the key controlling parameter that governs this rather complex problem is remarkably simple; it is, the ratio of N_f/N_g. If N_f/N_g is used as the normalization factor, we see that phase diagrams from different hairy nanoparticles and polymer melts must superimpose into one curve as observed experimentally. The phase diagram, after such normalization, will be independent of polymer species and would be universally applicable. Other factors, including the hair-grafting density σ and the particle core radius R_0, are not nearly as significant as N_f/N_g in this case. The pre-factor $(a/R_0\sigma\upsilon^2)^{1/3}$ in Equation (17) is expected to be near unity, because the 1/3 power minimizes the roles σ and R_0 play in this problem. For a particle radius of 10 nm and $a/R_0 = 0.05$, with grafting density $\sigma = 0.2$ and $\upsilon = 0.6$ we estimate $(a/R_0\sigma\upsilon^2)^{1/3} = 0.9$. The shift factor $\kappa = 1.2$ observed experimentally might be due to the term $(a/R_0\sigma\upsilon^2)^{1/3}$. Since the interaction potentials between hairy particles are entropic in nature, the phase diagram of hairy nanoparticles in polymer melts is not expected to be sensitive to temperature changes. This conclusion is also observed experimentally.

4.2. Mechanical nonlinearity and critical phenomena

To interpret the surprising connection between the dynamical nonlinearity and the phase separation of the particle-filled system, we need to turn our attention to the fundamental physics of critical phenomena. Generally speaking, near the critical point of a system, there are large fluctuations in composition from point to point. This is observed macroscopically through the phenomenon of opalescence divergence [58–61]. If the nucleation-induced phase separation is sufficiently suppressed, the phase separation of this system will occur via a spinodal decomposition mechanism. Our system in fact follows this mechanism because the nanoparticles of our study do not crystallize at any present condition. As a result, the phase separation produces transiently connected networks. Because the nano-sized hairy particle has a long thermal diffusion time in an entangled polymer matrix [62], the development of networks will virtually arrest right after the initial stage of the spinonal decomposition [63]. The grain size or the correlation length ζ of the formed structure will then scale similarly as the wavelength of the fastest growing density fluctuation λ does near the critical point of the phase separation:

$$\zeta = \zeta_0\varepsilon^{-g/2} \tag{18}$$

where $g = 1.24$ is the critical exponent, ζ_0 is the critical amplitude and $\varepsilon = (M_f - M_f^c)/M_f^c$ is the distance to critical point.

The relaxation rate of the formed structure is expected to be extremely small. This can be understood from an Einstein equation between the relaxation rate $(1/\tau_0)$ and the size ζ of an object, i.e.,

$$1/\tau_0 = c/\zeta \tag{19}$$

where c is constant. A rough estimate of the rate $1/\tau_0$ can be made from the Stokes–Einstein equation $1/\tau_0 = kT/6\pi\eta\zeta$. For a PBD viscosity of $\eta = 10^5$ Pa and a grain size of $\zeta = 1$ μm (typical values for system studied here), we estimate $1/\tau_0 \sim 10^{-7}\,s^{-1}$.

However, under shear we expect a drastic increase of the structural relaxation rate $1/\tau$ to $10\,s^{-1}$. The reason is that during dynamic shear measurements large strains may disrupt the critical fluctuation-induced structures and force the system to explore different configurations. The structural relaxation time τ occurring at large strains may be described by a Bingham-type equation [64–66]:

$$1/\tau = 1/\tau_0 + K\dot{\gamma}^m \cong K\dot{\gamma}^m \tag{20}$$

where $\dot{\gamma}$ is the strain rate. K and m are constants. In his original proposal, Bingham wrote viscosity η instead of τ and assumed $m = 1$ in Equation (20). Since $\eta \sim \tau$, the nature of this substitution is the same. Here letting $0 \le m \le 1$ would broaden applications.

To simplify our argument, the mechanical response of our system is assumed to follow the description of a nonlinear Maxwell spring–dashpot elements [67] such as

$$\dot{\sigma} = E\dot{\varepsilon} - E\sigma/\eta \tag{21}$$

plus a process-dependent viscosity [68], such as, that described by Equation (20). In this model, σ and ε are stress and strain, respectively. $\dot{\sigma}$ and $\dot{\varepsilon}$ are stress and strain rates, respectively. E is the spring constant. At an oscillatory strain $\gamma(t) = \gamma e^{i\omega t}$, this model gives the shear rate dependence of the storage modulus G' as [68,69]:

$$\frac{G'(\gamma) - G'_\infty}{G'_0 - G'_\infty} = \frac{1}{1 + \left(\dot{\gamma}/\dot{\gamma}_y\right)^{2m}} \quad \text{when } t_0 \text{ is large} \tag{22}$$

where $\dot{\gamma}_y$ is the critical shear rate which results in material yielding. G'_0 and G'_∞ are zero and large strain limiting values of G', respectively. Equation (22) gives rather similar predictions for the nonlinear effect as that proposed by Kraus [70]. The strain rate $\dot{\gamma}$ in Equation (22) can be re-written as the strain amplitude γ if the oscillatory shearing is carried at a constant frequency ω.

Suppose "yielding" means that the modulus of the material upon shearing is sharply reduced by about 1/2 or less. This would correspond to a certain relaxation time at the yielding point, τ_y. Without losing generality, let us consider $\tau_0/\tau_y = \theta$. Here $\theta > 1$ is a constant and its value is chosen with the definition of yielding. Thus, the yielding shear rate $\dot{\gamma}_y$ can be expressed, through Equations (18)–(20), as a function of the distance to the phase separation critical point.

$$\dot{\gamma}_y^m = \frac{\theta - 1}{K\tau_0} = \frac{(\theta - 1)c}{K\zeta} = \frac{(\theta - 1)c}{K\zeta_0}\varepsilon^{2/g} \tag{23}$$

This result suggests that the strain-induced nonlinearity, as observed in the system, is expected to be linked to the details of critical phenomena. The physical picture is that as the system approaches the critical point, large fluctuations in particle composition will result in a formation of transit networks in the system. Under shearing the structural relaxation time of the system will drastically decrease. As a result, the mechanical response of the system becomes nonlinear. Because $\dot{\gamma}_y \sim \varepsilon^{2/gm}$ gets smaller as ε approaches zero, the system will in fact become weak mechanically when it is near the critical point. Thus, the nearer the system is to the critical point, the more nonlinear the mechanical response of the system will be.

A calculation of G' vs. γ as a function of the distance to the-critical point using Equations (22) and (23) is plotted in Fig. 12. Equation (23) predicts that the nonlinearity will reach a maximum at the critical point when $\gamma_y = 0$. The calculated result agrees qualitatively well with that observed experimentally. Our observation shows that the maximum is located slightly inside the two-phase regime. Nevertheless, this agreement is remarkable considering the simplifications made in the above theoretical analysis.

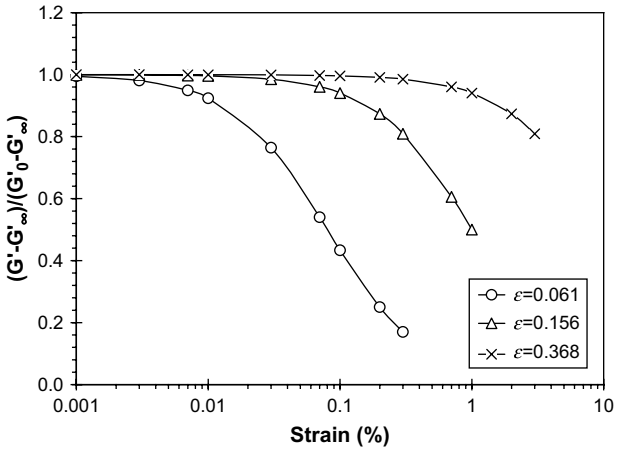

Fig. 12. A theoretical calculation of G' as a function of γ and the distance to the critical point ε. Results are calculated according to Equations (22) and (23) using $m = 0.6$, $g = 1.24$, and $(\theta - 1)c/K_{\tau 0} = 20$.

5. Conclusion

In this contribution we have reported on the phase behavior of polymeric hairy nanoparticles in polymer melts of chemically identical chains as function of both molecular weight and volume fraction. When the polymer melt is made of short chains, the interaction between the particles is always repulsive, and the suspension is transparent. When the polymer melt is made of long polymer chains, the interaction between particles is always attractive, and the suspension is opaque. Between the two extremes there is a clear transition from a transparent solution to an opaque suspension. Remarkably, the shape of the phase diagram is mainly determined by the ratio of the chain length of the polymer melts to the chain length of the polymer hair grafted on the nanoparticles. The onset of phase separation occurs when the chain length of the polymer melt is about twice as large as the chain length of the polymer hair grafted on the nanoparticles. Other factors, including the hair density and the particle diameter, are not nearly as significant as the above chain length ratio. In addition, the phase behavior of various hairy particles in a number of polymer melts can be unified into one universally applicable graph. Furthermore, there is a strong connection between the rheological dynamics of particle-filled systems and the thermodynamics of the phase separation behavior. The strain-induced nonlinearity in a particle-filled system appears to share the same physics as the critical phenomena. Our recent discovery of critical fluctuations in carbon black filled compounds might be due to the same mechanism [71].

References

[1] Davis CC, Blake JT. The chemistry and technology of rubber. New York: Reinhold Publishing; 1937.
[2] Blow CM. Rubber technology and manufacture. London: Butterworth & Co. Ltd.; 1971.
[3] Morton M. Rubber technology. Florida: Robert E. Krieger Publishing; 1981.
[4] Manson JA, Sperling LH. Polymer blends and composites. New York: Plenum Press; 1976.
[5] Krom J, Wang Xr. Nano-particle preparation and applications. USP6437050; 2002.
[6] Wang Xr, Foltz VJ. J Chem Phys 2004;16:121.
[7] Wang Xr, Foltz VJ, Sadhukan P. Crystalline polymer nano-particles. USP6689469; 2004.
[8] Wang Xr, Ozawa Y, Hall JE. Polymeric nano-particles of flower-like structure and applications. USP7205370; 2007.
[9] Wang Xr, Foltz VJ. Multi-layer nano-particle preparation and applications. USP6872785; 2005.
[10] Wang Xr, Hall JE, Warren S, Krom J, Magistrelli JM, Rackaitis M, et al. Macromolecules 2007;40:499.
[11] Wang Xr, Bohm GGA. Nano-sized inorganic metal particles, preparation thereof, and application thereof in improving rubber properties. US Pub 2007/0161754A1; 2007.
[12] Wang Xr, Lin CJ, Hall J, Warren S, Krom J, Kondo H, et al. Nano-particle preparation and applications. USP6956084; 2005.
[13] Wang Xr, Hall JE, Bohm GGA, Lin CJ. Nano-sized polymer–metal composites. USP7112369; 2006.
[14] Wang Xr, Rackaitis M, Foltz VJ, Kelly ED, Yan Y-Y. Non-spherical nanoparticles made from living triblock polymer chains. US Pub 2007/0149649A1; 2007.
[15] Wang Xr. Polymer nano-strings. USP6875818; 2005.
[16] Wang Xr, Foltz VJ, Sadhukhan P. Nanoparticles with controlled architecture and method thereof. US Pub 2007/0142559A1; 2007.
[17] Warren SM, Wang Xr. Amphiphilic polymer micelles and use thereof. US Pub 2005/0228074A1; 2005.
[18] Wang Xr, Sadhukhan P. J Electron Microsc 2007;56(6):209.
[19] Lapra A, Gandon PS, Varagniat F. Elastomer composition which is reinforced with a functionalised polyvinylaromatic filler. WO2006069793; 2006.
[20] Ziser T, Heiliger L, Fruh T, Obrecht W. Microgels in crosslinkable organic media. US Pub 2005/0182158A1; 2005.
[21] Obrecht W, Wrana C. Microgel-containing vulcanizable composition based on hydrogenated nitrile rubber. US Pub 2007/0135579A1; 2007.
[22] Castner ES. Emulsion particles as reinforcing filler. USP7217775; 2007.
[23] Xie FA, Zheng L, Casyner ES. Rubber composition containing resinous nano-particles. USP7071246; 2006.
[24] Zheng L, Castner ES, Materne TFE. Hairy polymeric nanoparticles. US Pub 2005/0203248; 2005.
[25] Lean JT, Caster ES. Core-shell polymer particles. USP6777500; 2004.
[26] Wijmans CM, Zhulina EB, Fleer GJ. Macromolecules 1994;27:3238.
[27] Shull KR. Macromolecules 1996;29:2658.
[28] Ligoure C. Macromolecules 1996;29:5459.
[29] Brown HR, Char K, Deline VB. Macromolecules 1990;23:3383.
[30] Witten TA, Leibler L, Pincus PA. Macromolecules 1990;23:824.
[31] Milner ST, Witten TA, Cates ME. Macromolecules 1988;21:2610.
[32] Milner ST, Wang Z-G, Witten TA. Macromolecules 1989;22:489.
[33] Gay C. Macromolecules 1997;30:5939.
[34] Semenov AN. Macromolecules 1992;25:4967.
[35] Ferreira PG, Ajdari A, Leibler L. Macromolecules 1998;31:3994.
[36] Clarke J, Vincent BJ. Colloid Interface Sci 1981;82:208.
[37] Clarke J, Vincent BJ. Chem Soc Faraday Trans 1981;77:1831.
[38] Cowell C, Li-In-On FKR, Vincent BJ. Chem Soc Faraday 1 1978;74:337.
[39] Vincent B, Luckham PF, Waite FAJ. Colloid Interface Sci 1980;73:508.
[40] Hasegawa R, Aoki Y, Doi M. Macromolecules 1996;29:6656.
[41] Semenov AN. Macromolecules 1993;26:2273.
[42] Borukhov I, Leibler L. Macromolecules 2002;35:5171.
[43] Gast AP, Leibler L. Macromolecules 1986;19:686.
[44] Gast AP, Leibler L. J Phys Chem 1985;89:3947.
[45] Matsen MW. Macromolecules 1995;28:5765.
[46] Noolandi J, Hong KM. Macromolecules 1983;16:1443.
[47] Braun H, Rudolf B, Cantow H-J. Polym Bull 1994;32:241.
[48] Whitmore MD, Noolandi J. Macromolecules 1985;18:657.
[49] Halperin A. Macromolecules 1987;20:2943.
[50] Ball RC, Marko JK, Milner ST, Witten TA. Macromolecules 1991;24:693.
[51] Li H, Witten TA. Macromolecules 1994;27:449.
[52] Belyi VA. J Chem Phys 2004;121(13):6547.
[53] Edwards SF. Proc Phys Soc 1965;85:613.
[54] Flory PJ. Principles of polymer chemistry. Cornell: Cornell University Press; 1953.
[55] Leibler L, Ajdari A. In: Teramoto A, Kobayashi M, Norisue T, editors. Ordering in macromolecular systems. New York: Springer; 1994. p. 301.
[56] Broseta D, Fredrickson GH, Helfand E, Leibler L. Macromolecules 1990;23:132.
[57] de Gennes PG. Macromolecules 1980;13:1069.
[58] Hill TL. Statistical mechanics. New York: McGraw Hill Book; 1956.
[59] Binny JJ, Dowrick NJ, Fisher AJ, Newman MEJ. The theory of critical phenomena. Oxford University Press; 1992.
[60] Bruno TJ, Ely JF. Supercritical fluid technology. Florida: CRC Press; 1992.
[61] Ma SK. Modern theory of critical phenomena. New York: W.A. Benjamin; 1976.
[62] Wang Xr, Robertson CG. Phys Rev E 2005;72:031406.
[63] Cahn JW. J Chem Phys 1965;42:93.
[64] Bingham EC. Fluidity and plasticity. New York: McGraw-Hill; 1922.
[65] Barnes HA. J Non-Newtonian Fluid Mech 1999;81:133.
[66] An expression such as $1/\tau \cong K\dot{\gamma}^m$ can be further written as $\eta = \eta_\infty + K_\eta \dot{\gamma}^{-m}$. When $m = 1$, this can be easily recast as the Bingham equation by multiplying throughout the shear rate, so $\sigma = \sigma_0 + \eta_\infty \dot{\gamma}$, where the Bingham yielding stress $\sigma_0 = K_\eta$.
[67] Tobolsky AV. Properties and structure of polymers. New York: John Wiley & Sons; 1960.
[68] Lion A, Kandeley C, Haupt P. Rubber Chem Technol 2003;76:533.
[69] Wang Xr, Robertson CG. Europhys Lett 2007;79:18001. This reference also detailed the weakness of this simple model or Equation (20) as it cannot address the spectral hole-burning effects discovered recently in particle-filled systems.
[70] Kraus G. Appl Polym Symp J Appl Polym Sci 1984;39:75.
[71] Wang Xr, Rackaitis M. Europhys Lett 2006;75:590.